Generalized Deterministic Automated Design of Metasurface Antennas With 3-D Feeding Structures

Generalized Deterministic Automated Design of Metasurface Antennas With 3-D Feeding Structures

Lucia Teodorani, *Member, IEEE*, Marcello Zucchi, *Member, IEEE*, and Giuseppe Vecchi, *Life Fellow, IEEE*

***Abstract*— In this work we present an automatic, deterministic procedure to fully design an isotropic metasurface antenna, self-consistently including the metallic feeding structure. The impedance pattern has full spatial variability in two dimensions, to allow designs otherwise difficult. The design is based on the integral-equation formulation with a current-only approach, in which the surface impedance profile is derived only after the optimal current is found; this allows to avoid the solution of the forward problem at all steps of the algorithm, with a drastic reduction of computational resources; it does not require any assumption on the impedance profile. We also show how a 3-D feed can be accounted for in a hybrid scheme partially employing commercial 3-D simulation software. Application examples address center-fed circular metasurface antennas, in which the feed is not connected to the metasurface, and rectangular "strip-like" leaky wave antennas (LWAs) where the metasurface is electrically connected to the feeding surface. In all cases, the design is carried out up to the final layout, and the full antenna is simulated to verify the design.**

***Index Terms*— Impedance boundary conditions (IBCs), integral equations, metasurface antennas, method of moments, optimization.**

I. Introduction

METASURFACES, i.e., metamaterial-inspired surfaces composed of sub-wavelength elements, have emerged as a transformative paradigm in antenna design. They possess the ability to manipulate electromagnetic waves with unprecedented flexibility, offering many opportunities to tailor and enhance antenna functionalities.

The design of metasurface (MTS) antennas almost always employs the so-called impedance boundary condition (IBC) for approximating the local electromagnetic behavior of the surface through a single parameter, the surface impedance; the design then entails defining the spatial distribution of this parameter. Following this, the impedance is locally implemented by means of properly shaped unit cells. This two-step, multiscale approach allows to address the design of electrically large antennas, keeping the overall complexity under control.

Initially, methods for the design of metasurface antennas were targeted to circular domains and considered only sinusoidally modulated profiles [1], [2]. These methods, based on analytical considerations, demonstrated the practical feasibility of designing large metasurface antennas, and paved the way for more general and sophisticated approaches. More recently, fully numerical schemes have enabled the analysis and design of shaped MTS antennas on circular domains and other boundaries [3], [4], [5], [6], [7], with various degrees of generality in the impedance profile.

The direct way to numerically address the design issue is an optimization of the impedance profile; however, IBC synthesis methods have emerged that seek for the optimization of the (equivalent) *current* on the metasurface [7], [8], [9], [10], [11], [12], [13], [14], [15] as an alternative to those directly seeking an impedance profile. The former methods will be called "current-only" here, and the latter impedance-based. Current-only methods enjoy a significantly lower numerical complexity than the impedance-based, and are typically deterministic; in them, the sought-for impedance profile is obtained from the optimized current at the end of the process.

In particular, the current-only method presented in [7] is deterministic and can be proven to be of minimal complexity per-iteration. It allows arbitrary spatial variation of the impedance, without a priori knowledge on the targeted IBC profile (as opposed to, e.g., methods tailored to sinusoidally modulated MTS antennas, which require specific parameterizations [5], [6], [16]). The inputs are the geometry of the IBC surface, the definition of the feed, and the radiation pattern mask constraints.

The design of the feeding structure is usually carried out independently of that of the metasurface, with the main objective of maximizing the power excited in the appropriate surface wave [1], [17]. Its effect is then included in the design by means of the incident field, i.e., the field radiated by the feed in isolation; this procedure does not account for the feed–metasurface interaction. A very recent contribution [6] has addressed the full wave feeder modeling in the impedance-based optimization (as opposed to the present interest in current-based); it employs a physics-based specialized parametric impedance profile (as opposed to the present search

Received 11 January 2024; revised 27 June 2024; accepted 31 July 2024. Date of publication 18 September 2024; date of current version 30 October 2024. This work was supported by the Italian Ministry of Research through the Project "METEOR" under Grant PRIN 2020EY2LJT. *(Corresponding author: Lucia Teodorani.)*

The authors are with the Department of Electronics and Telecommunications, Politecnico di Torino, 10129 Turin, Italy (e-mail: lucia.teodorani@polito.it; marcello.zucchi@polito.it; giuseppe.vecchi@polito.it).

Color versions of one or more figures in this article are available at https://doi.org/10.1109/TAP.2024.3457149.

Digital Object Identifier 10.1109/TAP.2024.3457149

for a general impedance profile). As demonstrated there, a proper, self-consistent modeling of the feeding structure is important for a correct estimation of the (peak) gain of the metasurface antenna.

In this work, we generalize the method presented in [7] to encompass a specified feeding structure in the current-only inverse design of the metasurface antenna. This results in the fully self-consistent design of the entire metasurface antenna, and the ability to find the necessary impedance profile without a priori guesses. The synthesis algorithm presented in this article is restricted to isotropic metasurfaces; an extension to the design of anisotropic antennas is currently being developed. We observe that the proposed method is more general than our present emphasis on feeding structures. In fact, the PEC regions can have any function, not just feeding; nevertheless, this constitutes the most relevant case in practical designs. We not only address center-fed metasurface antennas, but also edge-fed "strip-like" leaky wave antennas (LWAs), in which the feed is electrically connected to the IBC part; this last case is hardly addressable without the present self-consistent treatment. We will also demonstrate the importance of leaving full spatial variability in the sought-for impedance pattern when addressing design instances where a guess of the solution is not readily available.

To the best of our knowledge, this is the first time that the feed structure is addressed into a current-only design method, with full spatial variability of the impedance pattern; also, this is the first time that a feeding structure electrically connected to the metasurface is considered.

Preliminary results relative to the present topic have been submitted as a conference paper [18]; this is the first account of the method, of its theory and implementation.

This article is organized as follows. In Section II, the mathematical formulation of the electromagnetic problem is outlined. Section III presents the details of the proposed self-consistent current-based design algorithm, with focus on the types of feed that can be handled. In Section IV, application examples are provided to validate the approach. In particular, two classes of antennas will be considered: a circular antenna excited by a coaxial aperture in the ground plane, and a rectangular, "strip-like" antenna fed at one edge by a coaxial-to-microstrip transition. For each case, a comparison of the performance with and without self-consistent modeling of the feed is given, in order to highlight its importance in practical scenarios. Finally, conclusions are drawn in Section V.

II. Forward Problem

In the analysis of metasurface antennas, the geometry can be divided into two distinct regions (Fig. 1): the surface $\mathcal{S}_{\text{PEC}}$ which contains all metallic portions (e.g., the feeding structure), and the surface $\mathcal{S}_{\text{IBC}}$ on which the IBC applies. This condition links the tangential electric field to the jump of the tangential magnetic field through the surface impedance tensor $\overline{\overline{\boldsymbol{Z}}}$ [19]

$$\boldsymbol{E}_{\tan} = \overline{\overline{\boldsymbol{Z}}} \cdot \left[\hat{\boldsymbol{n}} \times (\boldsymbol{H}^{+} - \boldsymbol{H}^{-})\right]. \tag{1}$$

In this work, as in [7], we will consider only a *scalar impedance*, i.e., $\overline{\overline{\boldsymbol{Z}}} = Z\,\overline{\overline{\boldsymbol{I}}}$ (where $\overline{\overline{\boldsymbol{I}}}$ is the identity tensor).

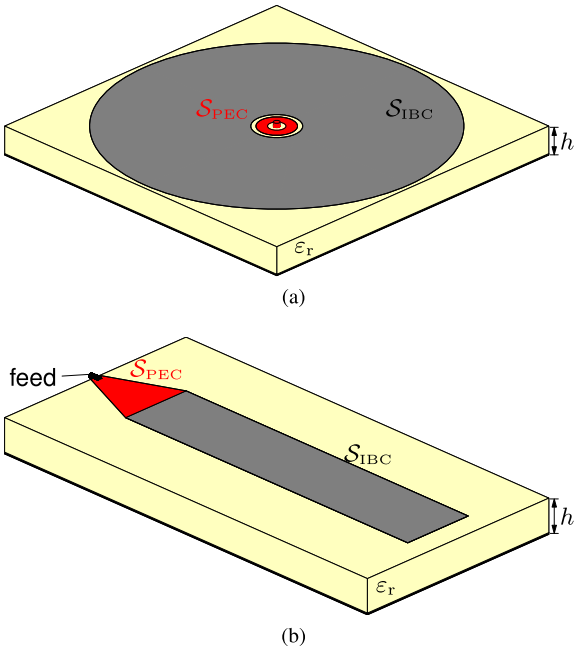

Fig. 1. Examples of two geometries of metasurface antennas. (a) Center-fed circular antenna. (b) Edge-fed "strip-like" antenna.

By introducing the equivalent current density

$$\boldsymbol{J} = \hat{\boldsymbol{n}} \times \left(\boldsymbol{H}^{+} - \boldsymbol{H}^{-}\right) \tag{2}$$

the electromagnetic problem is formulated as an *Electric Field Integral Equation*

$$\left[\boldsymbol{E}_{\text{inc}}(\boldsymbol{r}) + \mathcal{L}\boldsymbol{J}(\boldsymbol{r})\right]_{\tan} = \begin{cases} Z(\boldsymbol{r})\,\boldsymbol{J}(\boldsymbol{r}), & \boldsymbol{r} \in \mathcal{S}_{\text{IBC}} \\ \boldsymbol{0}, & \boldsymbol{r} \in \mathcal{S}_{\text{PEC}} \end{cases} \tag{3}$$

where $\boldsymbol{E}_{\text{inc}}$ is the field radiated by the (independent) sources in the absence of the metasurface and all metallic (PEC) parts, and $\mathcal{L}$ is the electric field integral operator (EFIO) defined as

$$\mathcal{L}\boldsymbol{J}(\boldsymbol{r}) = \iint \overline{\overline{\boldsymbol{G}}}^{\text{EJ}}(\boldsymbol{r}, \boldsymbol{r}') \cdot \boldsymbol{J}(\boldsymbol{r}')\, \mathrm{d}S(\boldsymbol{r}') \tag{4}$$

where $\overline{\overline{\boldsymbol{G}}}^{\text{EJ}}$ is the multilayer dyadic Green's function for the (grounded or ungrounded) substrate [20]. In the following, we indicate with $\boldsymbol{J}_{\text{ibc}}$ and $\boldsymbol{J}_{\text{pec}}$ the current density $\boldsymbol{J}$ on the two regions $\mathcal{S}_{\text{IBC}}$ and $\mathcal{S}_{\text{PEC}}$, respectively.

For the numerical discretization, we adopt the usual method of moments approach with Galerkin testing: we consider a mesh given by a triangular tessellation of the whole antenna surface and we approximate the sought current $\boldsymbol{J}(\boldsymbol{r})$ as a linear combination of Rao–Wilton–Glisson (RWG) basis functions $\boldsymbol{\Lambda}_n$ [21] defined on the N internal mesh edges

$$\boldsymbol{J}(\boldsymbol{r}) = \sum_{n=1}^{N} I_n\, \boldsymbol{\Lambda}_n(\boldsymbol{r}). \tag{5}$$

In the following, we will denote by N the total number of RWG functions (i.e., on both IBC and PEC regions), and by N_{ibc} and N_{pec} the number of functions with support on $\mathcal{S}_{\text{IBC}}$ and $\mathcal{S}_{\text{PEC}}$, respectively. Thus, in its most general form, the forward (analysis) problem reduces to the linear system

$$\mathsf{V}_{\text{inc}} + \mathsf{L}\mathsf{I} = \mathsf{Z}\mathsf{I} \tag{6}$$

where the array I collects the RWG basis coefficients I_n and the remaining quantities are defined as

$$(\mathsf{L})_{mn} = \langle \boldsymbol{\Lambda}_m , \mathcal{L}\boldsymbol{\Lambda}_n \rangle \tag{7}$$

$$(\mathsf{Z})_{mn} = \langle \boldsymbol{\Lambda}_m , Z\boldsymbol{\Lambda}_n \rangle \tag{8}$$

$$(\mathsf{V}_{\text{inc}})_m = \langle \boldsymbol{\Lambda}_m , \boldsymbol{E}_{\text{inc}} \rangle \tag{9}$$

where $\langle \boldsymbol{a} , \boldsymbol{b} \rangle = \int \boldsymbol{a} \cdot \boldsymbol{b} \, \mathrm{d}S$ is a symmetric bilinear form. It follows from (3) that, for test functions that lie on $\mathcal{S}_{\text{PEC}}$, $Z = 0$ and the corresponding matrix entries (8) are equal to zero. The interaction between the IBC and PEC currents is better highlighted by recasting (6) as

$$\begin{bmatrix} \mathsf{V}^{\text{inc}}_{\text{ibc}} \\ \mathsf{V}^{\text{inc}}_{\text{pec}} \end{bmatrix} + \begin{bmatrix} \mathsf{L}_{\text{ibc}} & \mathsf{L}^{\mathsf{T}}_{\text{cpl}} \\ \mathsf{L}_{\text{cpl}} & \mathsf{L}_{\text{pec}} \end{bmatrix} \begin{bmatrix} \mathsf{I}_{\text{ibc}} \\ \mathsf{I}_{\text{pec}} \end{bmatrix} = \begin{bmatrix} \mathsf{Z}_{\text{ibc}} & \mathsf{0} \\ \mathsf{0} & \mathsf{0} \end{bmatrix} \begin{bmatrix} \mathsf{I}_{\text{ibc}} \\ \mathsf{I}_{\text{pec}} \end{bmatrix} \tag{10}$$

where:

1) I_{ibc} and I_{pec} collect the RWG coefficients of $\boldsymbol{J}_{\text{ibc}}$ and $\boldsymbol{J}_{\text{pec}}$, respectively;
2) $\mathsf{V}^{\text{inc}}_{\text{ibc}}$ and $\mathsf{V}^{\text{inc}}_{\text{pec}}$ gather the coefficients of the projected incident field on the two regions;
3) the two square matrices L_{ibc} ($N_{\text{ibc}} \times N_{\text{ibc}}$) and L_{pec} ($N_{\text{pec}} \times N_{\text{pec}}$) represent the self-interaction of the two regions; and
4) the rectangular matrix L_{cpl} ($N_{\text{pec}} \times N_{\text{ibc}}$) identifies the coupling between the IBC and PEC regions.

The far-field can be computed from the current via the *radiation operator* $\mathcal{R}$

$$\mathcal{R}\boldsymbol{J}(\hat{\boldsymbol{r}}) = \frac{k_0}{2\pi \mathrm{j}} \iint \overline{\overline{\boldsymbol{G}}}^{\text{ff}}(\hat{\boldsymbol{r}}, \boldsymbol{r}') \cdot \boldsymbol{J}(\boldsymbol{r}') \, \mathrm{d}S(\boldsymbol{r}') \tag{11}$$

where $\overline{\overline{\boldsymbol{G}}}^{\text{ff}}(\hat{\boldsymbol{r}}, \boldsymbol{r}')$ is the multilayer far-field tensor [22] and the unit vector $\hat{\boldsymbol{r}}(\theta, \varphi)$ identifies the direction of radiation in spherical coordinates.

III. Self-Consistent Current-Only Inverse Design With Specified Feed

A. Requirements

The inputs to the design process are the specification of the substrate, the definition of the surface geometry, and of the source, i.e., the specification of the incident field. The definition of the geometry also involves the specification of the PEC structures, that may be planar or 3-D (see Fig. 1).

The goal of the design process is an impedance profile that, for the given incident field:

1) radiates a field pattern obeying the specifications (pattern masks); and
2) is physically realizable.

To obtain a physically realizable impedance, we must enforce that the metasurface be locally *passive* and *lossless*, and that the synthesizable reactance values fall within the technologically feasible range.

Far-field specifications are of the *mask type*, i.e., defined via *inequalities* for each considered far-field direction. These constraints must typically be expressed in terms of directivity or gain.

B. Self-Consistency

The current-based design method presented in [7] formulates the problem in such a way that it involves *only* the equivalent current on the IBC—not the impedance. This avoids the solution of the forward problem (6) at each step; instead, only the computation of the on-surface and radiated fields is required, with complexity $O(N \log N)$.

The self-consistent inclusion of the PEC structure (e.g., the feed) implies that the design algorithm must look for a *pair* of currents ($\boldsymbol{J}_{\text{ibc}}$, $\boldsymbol{J}_{\text{pec}}$) such that:

1) *together* they satisfy radiated field specifications,
2) on the IBC region, $\boldsymbol{J}_{\text{ibc}}$ satisfies IBC constraints (passivity, absence of losses, and feasibility range),
3) on the PEC region, $\boldsymbol{J}_{\text{pec}}$ satisfies the PEC boundary condition.

Note that the two parts of the current self-consistently interact with one another through the IBC-PEC coupling term L_{cpl} in (10).

C. Current-Only Optimization Framework for Metasurface Antenna Design

Here, we highlight only the most relevant features of the current-only design method in [7], as necessary to understand the proposed generalized design approach.

The total cost function that the algorithm aims to minimize can be expressed as

$$f = f_{\text{rad}} + f_{\text{ibc}} + f_{\text{pec}} \tag{12}$$

where each term is a functional, i.e., a scalar nonnegative function, of the surface current only.

Here, f_{rad} accounts for the radiated field requirements, and f_{ibc} encompasses the realizability constraints to be enforced on the IBC region (passivity, losslessness, and feasibility range). The term f_{pec} is added in order to enforce the PEC condition on the related surface. The radiated field and impedance terms are briefly discussed in Appendix A and B, respectively, while the term associated with the PEC condition will be introduced in detail in Section III-F. The considered minimization problem is intrinsically nonconvex (due to the passivity constraint); to limit the difficulties of nonconvexity, all functionals are expressed as fourth-degree multivariate polynomials in the current coefficients [11].

For the minimization of the cost function, a *nonlinear conjugate gradient* algorithm [23, p. 121] is employed. Given the large size of the problem, the numerical cost of computing the functional and its gradient at each iteration is an issue of paramount importance; hence, all operations are cast in such a way to be amenable to the use of fast factorizations, with $O(N)$ memory requirements and $O(N \log N)$ complexity per iteration. Therefore, the entire design process has a complexity of $O(N_{\text{iter}}^{\text{cur}} N \log N)$, where $N_{\text{iter}}^{\text{cur}}$ is the total number of iterations needed by the *current-only* algorithm to obtain the result. On the contrary, a classical *impedance-based* design requires, at each iteration, the solution of the linear system representing the electromagnetic problem for a given impedance distribution. In the most favorable scenario where fast iterative algorithms are used, this step has a

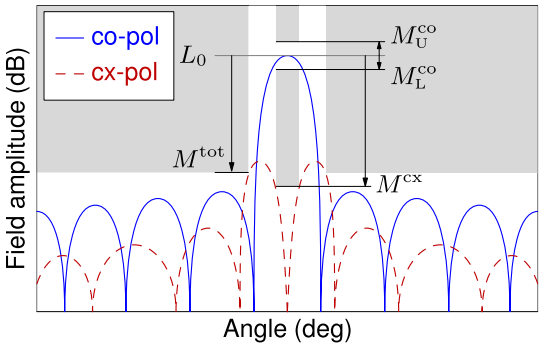

Fig. 2. Example of far-field specifications: main lobe co-pol upper mask $M_{\mathrm{U}}^{\mathrm{co}}$ and lower mask $M_{\mathrm{L}}^{\mathrm{co}}$, cross-pol mask M^{cx} and side lobes mask M^{tot}. All masks are defined relative to the reference level L_0, as indicated by the arrows.

complexity of at least $O(N_{\mathrm{sol}}\, N \log N)$ per iteration (where N_{sol} is the number of iterations needed by the iterative solver), resulting in a global complexity $O(N_{\mathrm{iter}}^{\mathrm{imp}}\, N_{\mathrm{sol}} N \log N)$ for the full design. In the latter case, the number of iterations $N_{\mathrm{iter}}^{\mathrm{imp}}$ is typically dependent on the global search algorithm employed for the optimization, and grows roughly exponentially with the number of parameters used to represent the impedance profile. This means that, for the optimization to be practically feasible, the number of parameters should be small (typically less than 10), forcing the designer to choose a priori the shape of the impedance profile (e.g., spiral modulation) based on the knowledge of the required radiation pattern. This is not always possible, as in the case of complicated shaped-beam patterns, limiting the generality of the *impedance-based* design process. Overall, a *current-only* approach offers more generality and a better scaling of the numerical complexity with an increasing number of degrees of freedom (and a larger antenna size, as a consequence).

D. Enforcement of Radiation Constraints

The radiated field is required to comply with upper and lower bounds for both the co- and cross-polarization components in the main beam

$$M_{\mathrm{L}}^{\mathrm{co}} \leq F^{\mathrm{co}} \leq M_{\mathrm{U}}^{\mathrm{co}} \tag{13}$$

$$F^{\mathrm{cx}} \leq M^{\mathrm{cx}} \tag{14}$$

and for the total amplitude in the sidelobe region

$$F^{\mathrm{tot}} \leq M^{\mathrm{tot}} \tag{15}$$

where F is the squared amplitude of the electric field component radiated in the far-field in a given direction. The masks are defined with respect to the reference level L_0, which can be fixed or given in terms of the radiation pattern (e.g., the amplitude in the direction of maximum radiation). The radiation requirements are summarized graphically in Fig. 2. By choosing a suitable value of L_0 which corresponds to the desired gain, the algorithm maximizes the radiated power for a given (input) power of the incident field.

Indicating with P_{inc} the power associated with the (given) incident field $\boldsymbol{E}_{\mathrm{inc}}$, the radiation pattern can be expressed in terms of the *realized gain* [24]

$$G_{\mathrm{r}}(\hat{\boldsymbol{r}}) = \frac{\left|\boldsymbol{E}(\hat{\boldsymbol{r}})\right|^2/\eta_0}{P_{\mathrm{inc}}/4\pi} \tag{16}$$

where η_0 is the free-space impedance, and $\boldsymbol{E}(\hat{\boldsymbol{r}})$ is the far-field radiated in a given direction. By invoking Poynting's theorem, and neglecting losses in the conductors and the substrate, one arrives at the following power balance equation:

$$P_{\mathrm{rad}} + P_{\mathrm{refl}} + P_{\mathrm{rim}} = P_{\mathrm{inc}} \tag{17}$$

where P_{inc} is the incident power (associated with the incident field), P_{rad} is the power radiated in far-field, P_{refl} is the power reflected toward the source, and P_{rim} is the residual surface wave power that is diffracted by the outer rim of the antenna (not modeled when considering an infinite dielectric). Therefore, maximizing the radiated power for a constant incident power [right-hand side of (17)] intrinsically minimizes the input reflection coefficient and the spurious contribution from the rim diffraction.

With these considerations, it is evident that the ability to include a real model of the feeding structure is crucial for the robustness of the optimization process.

E. Enforcement of IBC Constraints

The requirements for passivity and losslessness, the bounds on the synthesizable reactance values, and the scalarity condition can all be expressed in terms of fields as follows [7]:

$$\mathrm{Re}\left(\boldsymbol{E}_{\tan} \cdot \boldsymbol{J}^*\right) = 0, \tag{18}$$

$$X_{\mathrm{L}}|\boldsymbol{J}|^2 \leq \mathrm{Im}\left(\boldsymbol{E}_{\tan} \cdot \boldsymbol{J}^*\right) \leq X_{\mathrm{U}}|\boldsymbol{J}|^2, \tag{19}$$

$$\left|\boldsymbol{E}_{\tan} \times \boldsymbol{J}^*\right| = 0. \tag{20}$$

All the above conditions must hold locally for all $\boldsymbol{r} \in \mathcal{S}_{\mathrm{IBC}}$; in accordance with our cell-based spatial discretization scheme, we will enforce these conditions in the average sense over each mesh cell. The formulation of these functionals, including their explicit expression in terms of matrix operations, are reported in Appendix B.

Once the optimal current has been obtained through the optimization process, the impedance profile can be derived via (6) by expressing the unknown impedance profile as a linear combination of (scalar) basis functions, and solving the resulting linear system for the unknown impedance coefficients.

In the present work, we have employed basis functions which result in a piecewise constant impedance profile over the triangles of the mesh. This particular case, detailed in Appendix C, admits a closed-form solution for the impedance Z_i over the ith cell:

$$Z_i = \frac{\iint_{\mathcal{S}_i} \boldsymbol{E}_{\tan} \cdot \boldsymbol{J}^*\, \mathrm{d}S}{\iint_{\mathcal{S}_i} |\boldsymbol{J}|^2\, \mathrm{d}S}. \tag{21}$$

F. Enforcement of PEC Condition

We now discuss how to enforce the PEC condition coherently with the design algorithm presented in Section III-C. The condition of *Perfect Electric Conductor*

$$\boldsymbol{E}_{\tan}(\boldsymbol{r}) = \boldsymbol{0} \tag{22}$$

needs to be enforced everywhere on PEC surfaces, and this has to be done by a *functional*, i.e., a mapping from the N complex current coefficients into a *single* real nonnegative number. Opposed to this, we observe that Galerkin's testing of (22), corresponding to the PEC part of (3), leads to a *vector* of N_{pec} complex numbers.

The construction of the necessary functional can be done in two different ways, as detailed below. This functional will be denoted by $\rho^{\text{pec}}(\mathsf{I})$; it is related to the term f_{pec} in (12) through a weighting factor, $f_{\text{pec}} = w^{\text{pec}}\rho^{\text{pec}}(\mathsf{I})$. One must assign a specific value to this weighting factor (like those related to other functionals) in the intrinsically multiobjective optimization.

1) Cell-Wise Enforcement of PEC Condition: The first way to enforce the PEC condition (22) is through its average over individual cells. In passing from these multiple conditions to a real scalar, nonnegative number to be minimized, we face the same issue that arises when enforcing the local passivity condition (see [7], [11]): to avoid cancellations between positive and negative contributions, we must enforce the minimization of the sum of the *squares* of fields on individual cells. This results in expressing the functional as

$$\rho^{\text{pec}} = \sum_{i\in\mathcal{I}_{\text{pec}}} \rho_i^{\text{pec}} \tag{23}$$

with

$$\rho_i^{\text{pec}} = \frac{1}{A_i}\iint_{\mathcal{S}_i} |\boldsymbol{E}_{\tan}|^2 \,\mathrm{d}S. \tag{24}$$

Here, A_i is the surface area of $\mathcal{S}_i$, and $\mathcal{I}_{\text{pec}} = \{i \in \mathbb{N} \,|\, \mathcal{S}_i \subset \mathcal{S}_{\text{PEC}}\}$ collects the indices of mesh cells belonging to the PEC region.

We observe that this approach is totally coherent with the overall design approach in [7], summarized for convenience in Appendix B, which is based on local averages of the squared magnitude of fields and currents. We will refer to this formulation as "cell-wise" enforcement.

2) Edge-Wise Enforcement of PEC Condition: Another option is to consider explicitly the PEC condition (22) as in the standard EFIE [PEC part of (3)], recast here for ease of reference

$$\boldsymbol{E}_{\tan}(\boldsymbol{r}) = \left[\boldsymbol{E}_{\text{inc}}(\boldsymbol{r}) + \mathcal{L}\boldsymbol{J}(\boldsymbol{r})\right]_{\tan} = \boldsymbol{0}. \tag{25}$$

Upon discretization on the PEC region, (25) becomes

$$\boldsymbol{\epsilon}_{\text{pec}} = \mathsf{V}_{\text{pec}}^{\text{inc}} + \mathbf{L}_{\text{cpl}}\mathsf{I}_{\text{ibc}} + \mathbf{L}_{\text{pec}}\mathsf{I}_{\text{pec}} = 0. \tag{26}$$

In the above, the $N_{\text{pec}} \times 1$ vector $\boldsymbol{\epsilon}_{\text{pec}}$ is the EFIE error, and its norm—the EFIE residue—is the term that is minimized in any iterative solution of the associated problem.

In view of the above, we can thus define the PEC functional as the square of the PEC-restricted EFIE residue

$$\rho^{\text{pec}} = \left\|\boldsymbol{\epsilon}_{\text{pec}}\right\|^2. \tag{27}$$

We will refer to this formulation as "edge-wise" enforcement, as it derives directly from the EFIE discretized by RWG functions, which are edge-based. The main advantage of using the edge-wise enforcement approach (27) is that it can be in principle extended to model other kinds of boundaries, such as those that appear in the case of finite dielectric substrates.

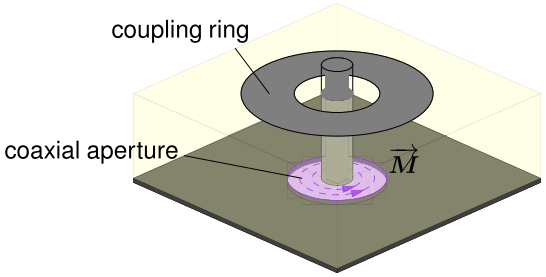

Fig. 3. Three-dimensional model of a coaxial feed through the ground plane; the specific geometry was inspired by [1]. The source is represented by the equivalent magnetic current $\boldsymbol{M}$ on the aperture.

Both formulations will be tested in Section IV in two self-consistent antenna designs that include a realistic feeding structure.

G. Computation

As for the method in [7], the present method allows to use fast algorithms for the field computations in the functional and the gradient computation alike. The PEC-related contributions to the functional all require only field evaluations, in turn expressible in terms of matrix-vector products; these can be computed with $O(N \log N)$ complexity using fast factorizations.

The same holds also for the PEC-related contributions to the gradient. In particular, if the PEC condition is enforced cell-wise via (23), the *complex gradient* [25] of the functional can be expressed as

$$\tilde{\nabla}\rho^{\text{pec}} = \mathbf{L}^{\text{H}}\mathbf{G}^{-1}\sum_{i\in\mathcal{I}_{\text{pec}}} \boldsymbol{\Gamma}_i \mathsf{V} \tag{28}$$

with $\mathsf{V} = \mathbf{G}^{-1}(\mathsf{V}_{\text{inc}} + \mathbf{L}\mathsf{I})$. Conversely, if edge-wise enforcement (27) is applied, one has

$$\tilde{\nabla}\rho^{\text{pec}} = \left[\mathbf{L}_{\text{cpl}} \;\; \mathbf{L}_{\text{pec}}\right]^{\text{H}}\boldsymbol{\epsilon}_{\text{pec}}. \tag{29}$$

In both cases, the matrix-vector products involving $\mathbf{L}^{\text{H}}$ (or sub-blocks of it) are required only once per gradient evaluation.

H. Handling of the Feed

The enforcement of the PEC condition is now applied to self-consistently include the PEC feeding structure into the automated design. In this work, two different types of feedings are considered.

1) Feeding from a waveguide (often a coaxial one) through the ground plane of the antenna, including both the vertical structure (most notably, a pin) and horizontal metal parts; this is depicted in Figs. 1(a) and 3 with reference to the cases analyzed in Sections IV-B and IV-C.
2) Feeding from the edge of the (planar) antenna, as depicted in Figs. 1(b) and 4; this case is described in Section IV-D.

The two classes differ mainly for the handling of the incident (forcing) field. We recall that this incident field is the one radiated by external sources in the structure without metallizations (other than the ground plane) and IBC.

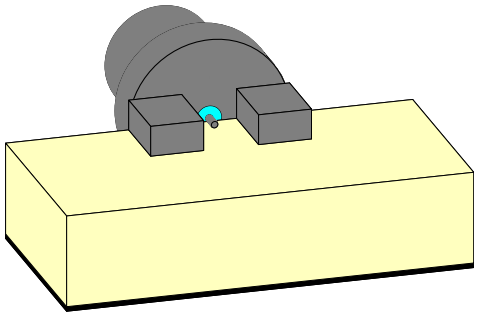

Fig. 4. Three-dimensional model of the coaxial feed used as source for the edge-fed antenna.

The effect of all metal parts (e.g., pin and matching rings) is self-consistently accounted for by the equivalent currents $\boldsymbol{J}_{\text{pec}}$ on the surface $\mathcal{S}_{\text{PEC}}$ of these parts. These currents are determined entirely *by the design process*.

It is indeed to be remarked that the optimization algorithm evolves the equivalent current over the IBC and PEC regions in such a way that, on completion, this current corresponds to a realizable surface impedance, generates a compliant radiated field *and* satisfies the PEC condition on the metal parts.

In the following, we will describe how the two considered types of feeding are handled in the design process.

1) Three-dimensional Feeding Through the Ground Plane: In this case, the source term is the equivalent magnetic current in the coaxial aperture at the level of the ground plane [26], [27], as seen in Fig. 3. In order to accelerate convergence, inside the iterative optimization instance the current $\boldsymbol{J}_{\text{pec}}$ on the PEC structures (vertical pin and matching rings) is initialized to the values, it would have in the absence of the IBC.

2) Three-dimensional Edge-Feeding: In case of edge-feeding, the real-life source is typically a coaxial connector placed horizontally on the top of the grounded dielectric substrate, with its outer conductor connected to the ground plane (see Fig. 4). Modeling of the 3-D coaxial feed in this case would be awkward and not exact in the underlying integral equation with infinite dielectric kernel. Hence, the modeling is done in two phases.

First, the coaxial connector is fully modeled inside a commercial electromagnetic solver, on a grounded dielectric substrate of infinite size, and without any top-layer metallization. The structure is simulated (full-wave) for a prescribed input port excitation and the radiated electric field is then extracted; this will constitute the incident field (this step corresponds to finding the incident field radiated by the modal current in the case of feeding through the ground in Section III-H1). This incident field is then used on the overall antenna, IBC and PEC parts.

Finally, we observe that, for this class of antennas, the design process without the feed is hardly meaningful, as opposed to the case of the center-fed circular (or similar) antennas. We will address a simplified, nonself-consistent version of the above in the example section (Section IV) and show its shortcomings.

IV. Application Examples

We address here the design of a standard circular metasurface antenna fed at its center, and of an elongated rectangular antenna ("strip-like") fed at one end (edge). These test cases are represented in Fig. 1(a) and (b), respectively. In the circular type [Fig. 1(a)], a vertical pin is placed at the center of the antenna, and an annular ring provides matching to the surrounding surface; in this case, the source is represented by the equivalent magnetic currents located at the insertion of the input coaxial cable into the ground plane, while a PEC constraint is imposed on both the pin and the annular ring. In the second case [Fig. 1(b)], the source of the incident field is on-surface, and the PEC region is introduced to represent the tapered section used to connect the feed to the radiating metasurface.

For the center-fed circular antenna, it is expected that the feeding structure may be well decoupled from the metasurface design [2], [28]; conversely, the edge-fed strip-like antenna has direct continuity of the PEC feeding structure and the radiating IBC; hence, the coupling is expected to be significant.

In both cases, two steps are required for the correct modeling of the feed in the optimization instance: the optimization of the geometry of the launching structure, and the extraction of the incident field $\boldsymbol{E}_{\text{inc}}$ to be given as input to the automated design method.

The results shown in this section are obtained as follows: from the optimum current, the impedance profile $Z(\boldsymbol{r})$ is retrieved, as indicated in Section III-E, keeping only its imaginary part. In the specific examples presented in this article, having established a priori the periodicity of the unit cells that will be used to physically implement the synthesized impedance, the triangular meshing of the antenna geometries is done in such a way that an exact number of triangular mesh cells fits inside a square unit cell of this "higher level" tessellation. Since the impedance that is synthesized by the automated design method is reconstructed on every triangular cell, this "conformal" meshing allows to compute the impedance corresponding to a square unit cell unequivocally as the average of the values of the synthesized impedance on the triangular mesh cells inside that square. The final impedance profile is therefore constant over square cells. Next, the actual solution is computed by solving the forward problem (6) for this impedance profile, the PEC parts, and the specified source field; the corresponding radiation pattern is then calculated. This means that the results take into account a possible efficiency reduction due to the impedance reconstruction process (from the optimized current). These final results are identified as "outputs of the design method."

After this consistency verification, the actual antenna is realized and simulated. The (scalar) impedance distribution is realized with patches; here, we use square patches throughout. The final test is the full-wave solution of the actual antenna, which is carried out using either the commercial solver CST Studio Suite [29] or an in-house MoM solver.

The design instances are carried out on a Desktop PC with Intel Core i9 processor and 64 GB RAM.

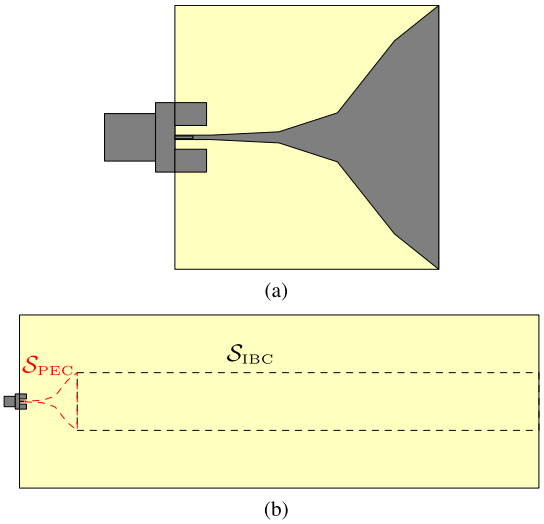

Fig. 5. Modeling of the realistic feed for the design of the edge-fed antenna (Section IV-D). (a) Coaxial connector and optimized tapered microstrip section. (b) Top view of the coaxial connector placed on the grounded dielectric substrate in absence of metallizations on the top layer. Dashed lines enclose the areas over which the incident field is evaluated and extracted to be given as input to the automated design method.

A. Feed Design

For both the feed geometries considered in this article, the definition of the layout and dimensions of the launching structures must be finalized ahead of the IBC design process.

For the circular antenna layout, the central pin height and the annular ring radius and width (see Fig. 3) are optimized using CST in order to minimize the reflection coefficient *and* maximize the radial power flow inside the dielectric substrate. Both objectives are important, since the mere minimization of S_{11} does not guarantee that the field is conveyed through the dielectric to the metasurface, rather than radiated in free space by the vertical pin.

For the edge-fed antenna, a proper tapered microstrip section must be designed to connect the coaxial feed to the actual metasurface. In particular, the tapered input section is optimized using CST in order to match the coaxial feed to the input impedance of a microstrip as wide as the metasurface "strip" transverse width. This choice for the optimization of the tapered section ensures a potential good matching between feed and metasurface, optimally launching the forward traveling wave. In fact, one has to keep in mind that our proposed automated design method will intrinsically try to minimize the reflection coefficient (as explained in Section III-D).

Once the dimensions of the tapered matching section have been finalized, $\boldsymbol{E}_{\rm inc}$ is retrieved by performing a full-wave simulation of the coaxial connector placed on the grounded dielectric substrate, in absence of any metallization, and extracting the field impinging over the entire structure layout (initial transition region plus IBC region), as explained in Section III-H2. This is exemplified in Fig. 5, that shows the optimized launching structure and the simulation setup for the extraction of the incident field for the dielectric substrate and working frequency of the design presented in Section IV-D.

B. Circular Metasurface With Broadside Pencil Beam

The design of a circular metasurface radiating a circularly polarized pencil beam is considered. A RO3003 dielectric substrate with $\varepsilon_r = 3$ and thickness 1.27 mm is chosen. The antenna has a radius of $6\lambda_0$ at the working frequency of 23 GHz, for a diameter of 156 mm. The reference geometry is shown in Fig. 1(a). The employed feed structure is shown in Fig. 3, and has been inspired by [1] and [2].

After the optimization of the launching structure and the determination of the incident field as described in Section IV-A, the bounds on the synthesizable impedance and the far-field mask-type constraints must be imposed. The desired far-field masks are shown in all figures reporting radiation patterns. For this design, we consider a capacitive reactance in the range $[-2000, -200]\ \Omega$, which can be implemented using square patch-type unit cells with a periodicity of 1.625 mm ($\approx\lambda_0/8$). The mapping between sheet reactance values and square patch dimensions is retrieved by performing normal-incidence scattering simulations of the constitutive unit cells, as done in [30]. An initial constant current with linear polarization is chosen on the IBC region, while for convergence purposes the initial $\boldsymbol{J}_{\rm pec}$ is set equal to the one that would flow on the feeding structure in absence the metasurface, as explained in Section III-H.

This design task is performed twice, using either the *cell-wise* or the *edge-wise* enforcement of PEC constraint, in order to test the effectiveness of both formulations. Finally, an alternative design case in which the launching structure is replaced by an ideal incident field is reported, to highlight the advantages of the proposed self-consistent inclusion of the realistic model of the feed in the overall performance of the designed antennas.

The number of RWG basis functions for the full geometry, including the launching structure, is $N = 44\,244$ ($N = 41\,776$ in the case of ideal incident field). The optimization of the full circular antennas (including the launching structure) took 1500 iterations, each requiring 7 s to complete, for a total running time of about 3 h for each case. The test design case with the ideal incident field required 500 iterations of 4 s each, for a total time of $\approx$33 min.

Due to the large size of the antenna and the considerable amount of mesh cells needed to obtain accurate results, the simulation of circular metasurfaces with a commercial solver is not possible with the hardware available to the authors; therefore, the actual antennas (with unit cells) are simulated using a MoM-based in-house solver.

1) Design With Cell-Wise Enforcement of PEC Constraint: The incident field, the optimum current, and impedance pattern returned by the automated design method applying the *cell-wise* PEC constraint formulation are shown in Fig. 6, while the resulting radiation pattern and its comparison to the one obtained simulating the complete actual antenna are pictured in Fig. 7. Only the far-field cut at $\varphi = 0°$ is reported as example, but the mask constraints were set on the whole 3-D upper hemisphere. A perspective view of the complete antenna, with square patches and central feeding structure, that has been

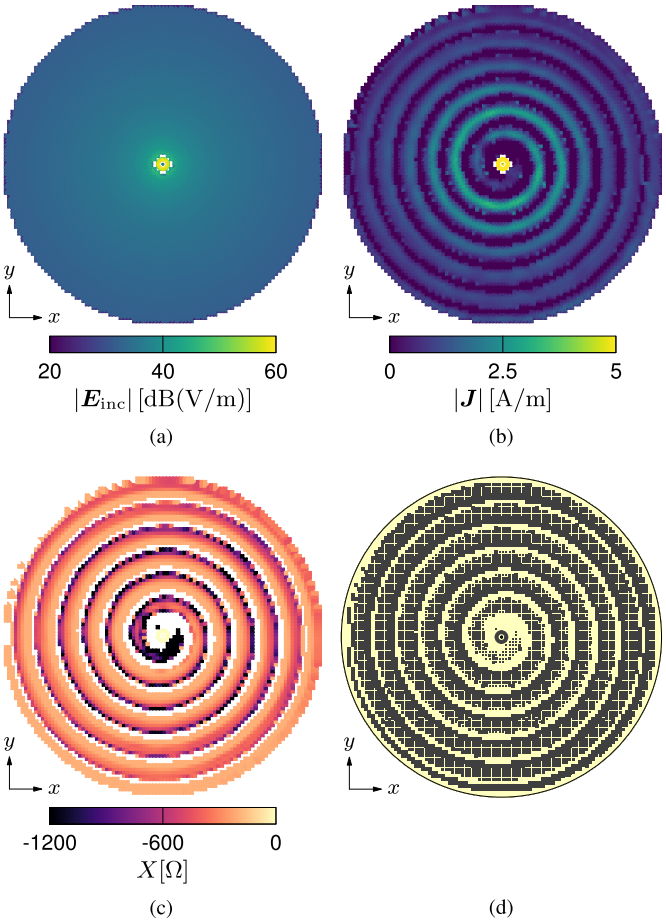

Fig. 6. Circular metasurface with pencil beam, design input/outputs using cell-wise enforcement of PEC constraint. (a) Incident electric field. (b) Optimum current density returned by the automated method. (c) Synthesized impedance pattern. (d) Implementation via square patches of the synthesized impedance.

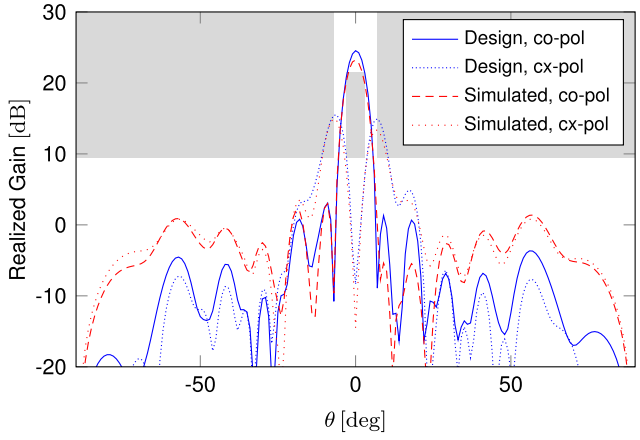

Fig. 7. Circular metasurface with pencil beam, full self-consistent design with cell-wise enforcement of PEC constraint: comparison between the far-field pattern due to the reconstructed equivalent currents (*Design*) and the one obtained with full-wave simulation of the complete antenna shown in Fig. 8 (*Simulated*).

simulated with the in-house MoM solver to verify the results of the design method is pictured in Fig. 8.

From Fig. 7, we can see that there is good agreement around the main beam between the expected and simulated radiation patterns, both in the co- and cross- polarization components.

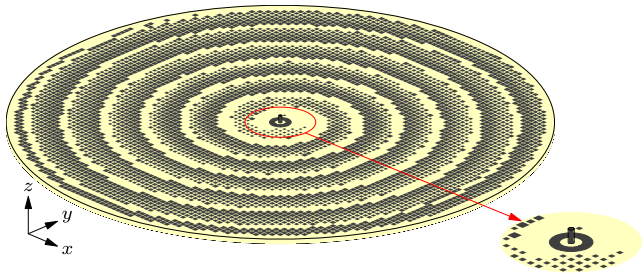

Fig. 8. Perspective view of the actual circular antenna, with square patches and central feeding structure, that has been simulated with the in-house MoM solver to verify the results of the design method in Section IV-B1.

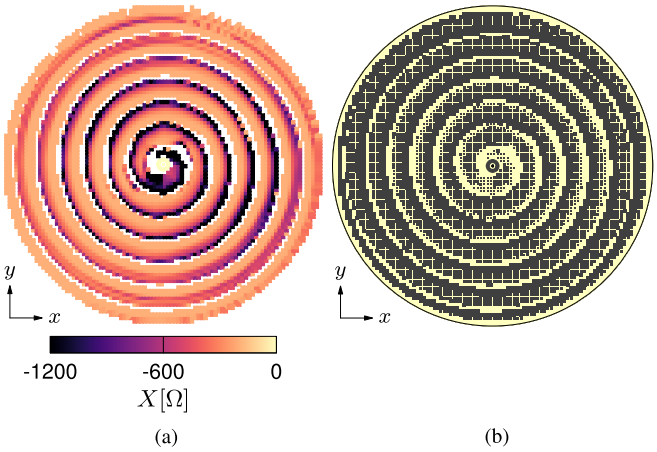

Fig. 9. Circular metasurface with pencil beam, full self-consistent design using edge-wise enforcement of PEC constraint. (a) Synthesized impedance pattern, and (b) its implementation via square patches.

However, the side lobes appear higher in the simulated pattern, although still quite low and following the shape of the design ones.

The simulated antenna exhibits a total efficiency of 81% and an aperture efficiency of 18%; these quantities are evaluated according to the definitions given in [24].

2) Design With Edge-Wise Enforcement of PEC Constraint: The same design is now carried out enforcing the PEC condition *edge-wise*. The synthesized impedance pattern and its implementation using square patches are shown in Fig. 9, while the comparison between the far-field predicted by the design method and the one obtained with full-wave simulation of the complete antenna is pictured in Fig. 10. The impedance pattern is very similar to the one obtained with *cell-wise* enforcement of the PEC constraint [see Fig. 6(c)]; the main discrepancy can be found near the central launching structure. On the other hand, there is excellent agreement between the expected and simulated radiation patterns also in the sidelobe region, while the achieved realized gain at broadside is the same as in the previous design. These results suggest that, for the circular geometry with central pin and annular ring, the *edge-wise* formulation may be slightly more effective in enforcing the PEC condition and the self-consistent evolution of the current density in these regions at every step of the optimization process. The total and the aperture efficiencies of the simulated antenna are 85% and 18%, respectively.

3) Design With Ideal Cylindrical Surface Wave: In order to demonstrate the advantage of including a realistic modeling of

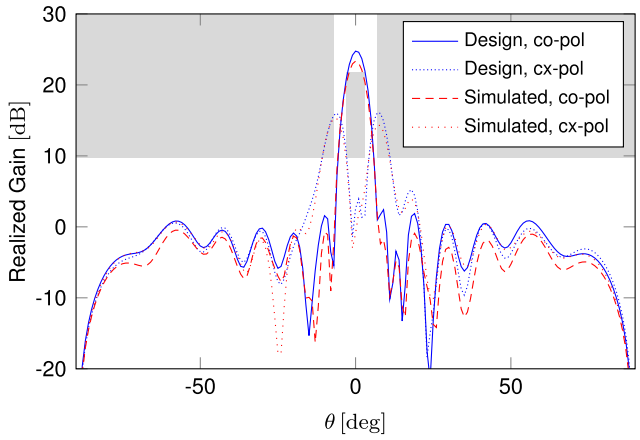

Fig. 10. Circular metasurface with pencil beam, full self-consistent design with edge-wise enforcement of PEC constraint: comparison between the far-field pattern due to the reconstructed equivalent currents (*Design*) and the one obtained with full-wave simulation of the complete antenna (*Simulated*).

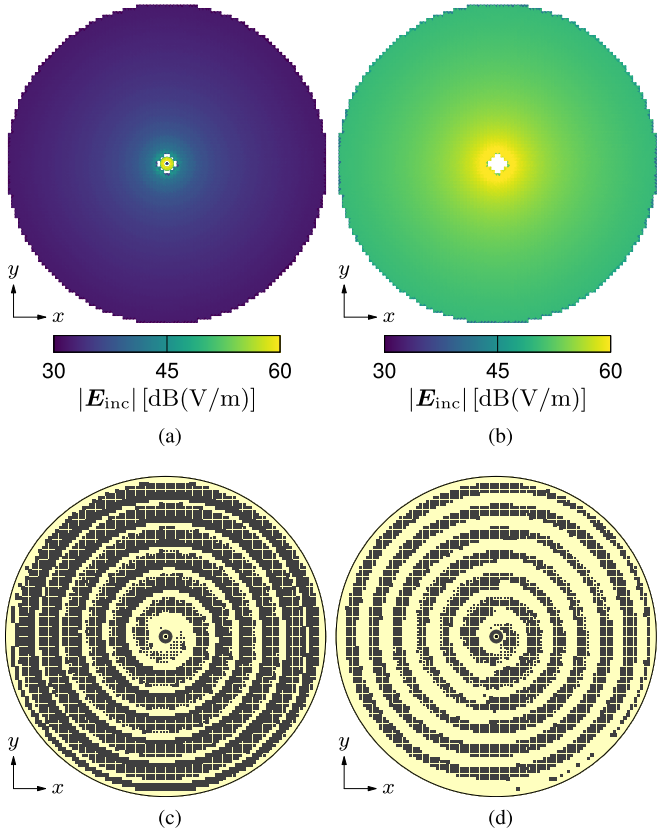

Fig. 11. Circular metasurface with pencil beam, comparisons between the self-consistent design with a realistic feed of Section IV-B1 and the one with a TM_0 approximate source. (a) Incident electric field, realistic feed (same of Fig. 6(a), different scale). (b) Incident TM_0 electric field. (c) Metallization pattern, realistic feed. (d) Metallization pattern, TM_0 source.

the feed in the design of circular metasurfaces, an alternative design case is presented in which the launching structure, comprising the central pin and the annular ring, is absent in the optimization instance, and the incident field is simply approximated with its asymptotic form as a TM_0 cylindrical surface wave, as it is commonly done in the literature [7], [31]. The TM_0 incident field is pictured in Fig. 11(b), while

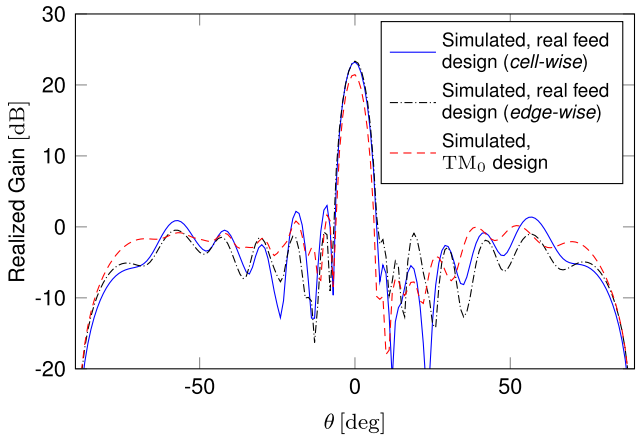

Fig. 12. Circular metasurface with pencil beam, comparison between the designs with full feed and approximate TM_0 incident field. The patterns are the simulations of the actual antennas in Fig. 11(c) and (d) that include the actual feed as in Fig. 8. Solid line: antenna designed considering the actual feed–cell-wise; dash-dotted line: antenna designed considering the actual feed–edge-wise; dashed line: antenna designed with a TM_0 incident field.

the complete geometry of the antenna designed starting from such field is shown in Fig. 11(d). The synthesized impedance pattern is very similar to the one obtained previously by properly modeling the launching structure [see Fig. 11(c) for a comparison with the design of Section IV-B1]; however, there are more empty areas (infinite impedance, no IBC) in the spiral distribution of patches, most likely due to the fact that the approximate TM_0 incident field decades less rapidly than the real one [see Fig. 11(a) and (b)] and it is thus still larger toward the edge of the circular area.

We now compare the performances of the three antennas: the one designed starting from a TM_0 incident field, and the ones designed with the accurate modeling of the feed (shown previously in Figs. 7 and 10). Fig. 12 shows the radiation patterns of the complete antennas depicted in Figs. 6(d), 9(b) and 11(d). It appears that using the approximate TM_0 incident field for the antenna design leads to a drop in the actual antenna realized gain of about 2 dB; in fact, the antenna designed starting from the ideal cylindrical wave shows a lower total efficiency of 66% and a smaller aperture efficiency of 15%. This proves the importance of considering the real 3-D feeding structure in the design of metasurface antennas.

C. Circular Metasurface With Multibeam Radiation

A more challenging design of a circular metasurface radiating a circularly polarized multibeam is carried out to test the performance of the proposed automated design method. The same substrate and launching structure of Section IV-B are employed to synthesize an antenna that radiates four beams in the directions given by $\theta = 45°, \varphi = \{45°, 135°, 225°, 315°\}$. An initial constant current with linear polarization is chosen, and the PEC constraint is enforced *cell-wise*. As in the previous cases, 1500 iterations of the optimization method were carried out, for a total running time of about 3 h.

The synthesized impedance pattern and its implementation using square patches are shown in Fig. 13, while the comparison between the far-field predicted by the design

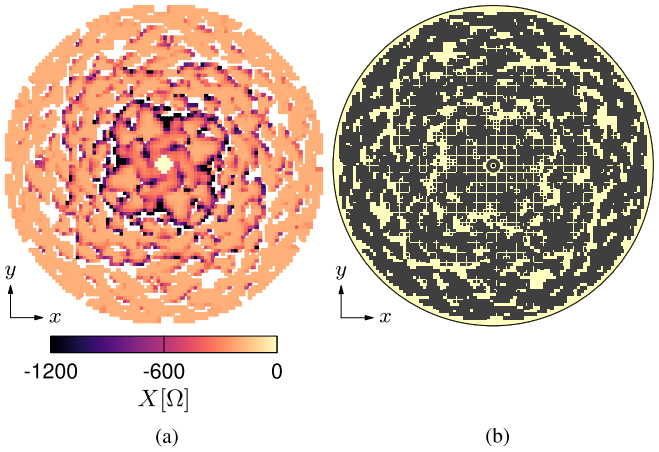

Fig. 13. Circular metasurface with multibeam, design outputs using cell-wise enforcement of PEC constraint. (a) Synthesized impedance pattern, and (b) its implementation via square patches.

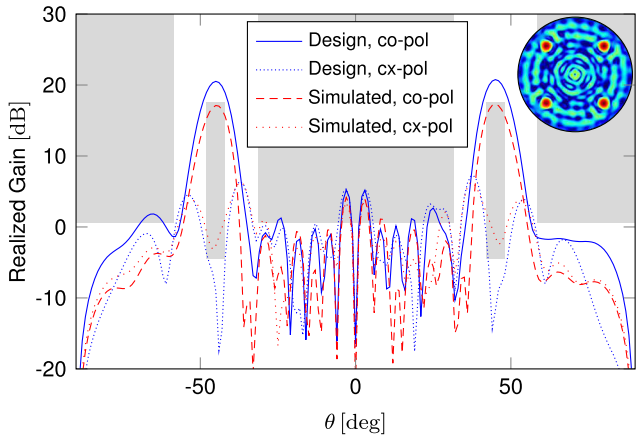

Fig. 14. Circular metasurface with multibeam, full self-consistent design with cell-wise enforcement of PEC constraint: comparison between the far-field pattern due to the reconstructed equivalent currents (*Design*) and the one obtained with full-wave simulation of the complete antenna (*Simulated*) in the plane $\varphi = 45°$. The inset shows the co-polarization pattern in the u-v plane.

method and the one obtained with full-wave simulation of the complete antenna is pictured in Fig. 14. Multibeam radiation is achieved without any a priori imposition on the shape of the impedance pattern. There is good agreement between the expected far-field pattern and the simulated one, with a drop of 3 dB in the peak simulated realized gain; this discrepancy may be due to inaccuracies in the full-wave simulation, given the large number of mesh cells required to obtain accurate results. The total efficiency of the simulated antenna is equal to 75%.

D. "Strip-Like" Rectangular Metasurface With Broadside Radiation

Another example of the application of the described numerical method is the design of a quasi-1-D LWA to achieve broadside radiation with inline feeding from one end. This is typically hard to obtain with conventional approaches [30], [32] due to the presence of an open stopband that leads to a nearly total reflection of the traveling wave [33]; hence, it is a very good test for the proposed method.

The reference geometry is the rectangular one shown in Fig. 1(b). A 2.286 mm-thick RO3006 substrate ($\varepsilon_r = 6.5$) is considered. The design frequency is 10 GHz. For "strip-like" metasurface antennas, the far-field mask-type constraints are set only in the $\varphi = 0°$ plane. The impedance constraints are based on the values that can be obtained using patch-type unit cells with a periodicity of 2 mm, for a total feasible reactance range of $[-10\,000, -150\,]\ \Omega$.

As already noted, the physical layout makes it virtually compulsory to include the feeding structure (at least the tapering section) in the design process. The launching structure has been inspired by [30]; its optimization is carried out as described in Section IV-A, and its final layout is shown in Fig. 5(a). The IBC region is a 30×240 mm rectangular area.

The current is initialized to an $\hat{\boldsymbol{x}}$-directed constant current which radiates broadside with linear polarization (which would not be physically realizable).

In the following, we examine the relevance of incorporating a realistic feed in the design of "strip-like" rectangular metasurface antennas, and the possible differences in using either the *cell-wise* or *edge-wise* enforcement of the PEC constraint. The number of degrees of freedom for the full geometry (IBC region and launching structure) is $N = 11\,116$. The optimization of the full rectangular antennas (including the launching structure) presented in Sections IV-D2 and IV-D3 took 20 000 iterations, each requiring 0.85 s to complete, for a total running time of about 4 h 40 min for each case.

1) Design Without Self-Consistent Modeling of the Launching Structure: We begin our analysis by considering a simplified, nonself-consistent description of the launching structure. For this (approximate) design case, the incident field is the one generated by the full launching structure, comprising the 3-D connector and the tapered section; the tapered section is left open-ended as show in Fig. 15. It is apparent that this is already a good approximation, since it takes the feeding mechanism into account and does not use an ideal incident field. On the other hand, only the IBC rectangular area $\mathcal{S}_{\text{IBC}}$ is considered (i.e., optimized) in the design, but not the PEC launching region $\mathcal{S}_{\text{PEC}}$ [see Fig. 15(a)]. This means that the tapered launching metal is nonself-consistently accounted for. In this case, the number of degrees of freedom is $N = 10\,665$ and the optimization process required 15 000 iterations of 0.48 s each, for a total running time of about 2 h.

Fig. 15(b) shows the incident electric field extracted from CST. Since the launching structure may generate (unwanted) radiation, it is necessary to consider also its contribution to the far-field as input to the design method [see Fig. 15(c)].

The optimum current synthesized by the automated method, the corresponding impedance pattern and its implementation with square patches are shown in Fig. 16. The empty areas in Fig. 16(b) indicate an open-circuit condition for the IBC, i.e., absence of metallization on the dielectric substrate.

The radiation pattern predicted by the automated design process is compared to the one obtained via full-wave simulation of the complete antenna in Fig. 17, together with the far-field masks imposed as targets in the optimization

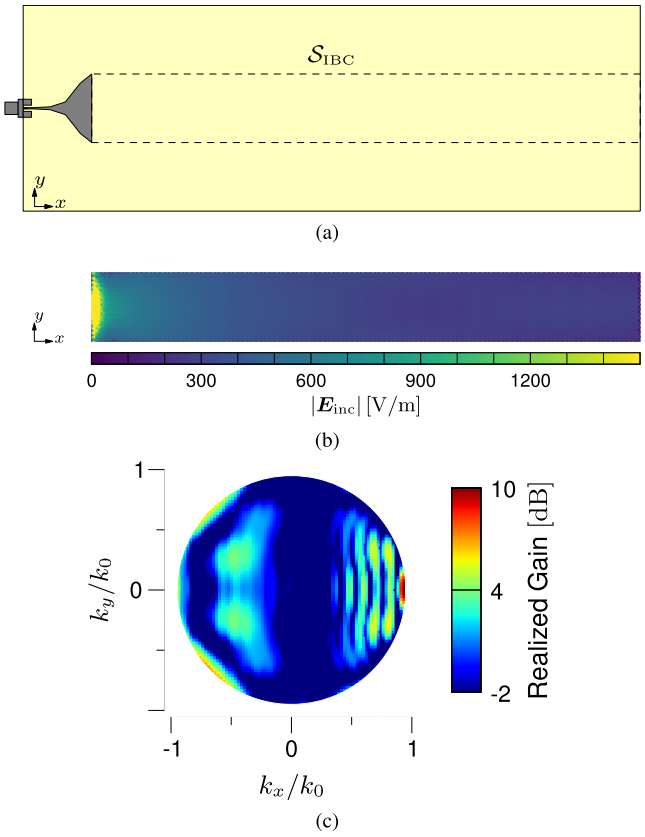

Fig. 15. Strip-like LWA, broadside radiation: design inputs for the case without self-consistent modeling of the PEC launching structure. (a) Setup for the simulation of the real antenna feed using CST, where the dashed lines enclose the area of extraction of the incident electric field ($\mathcal{S}_{\rm IBC}$). (b) Extracted incident electric field to be used in the design method in $\mathcal{S}_{\rm IBC}$. (c) "Input" far-field in the u-v plane, due to the radiation of the feed, i.e., associated with the "incident" field.

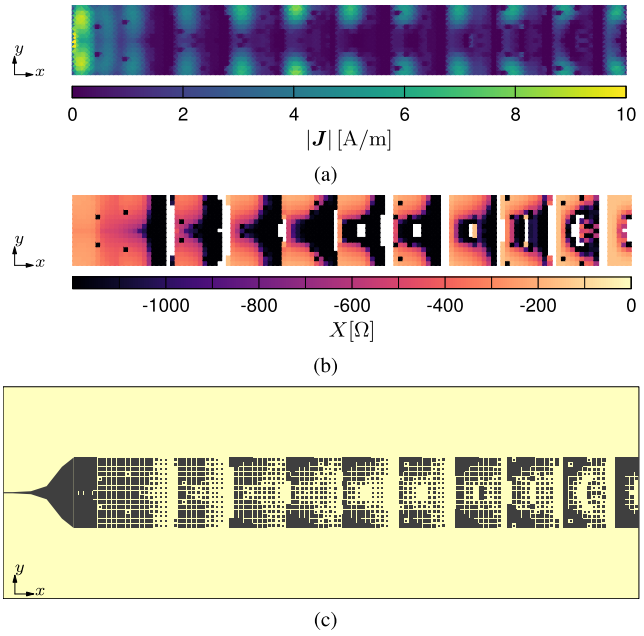

Fig. 16. Strip-like LWA, broadside radiation: design outputs for the solution without the self-consistent modeling of the launching structure. (a) Optimum IBC current density returned by the design method. (b) Impedance pattern corresponding to the optimum current in (a). (c) Implementation via square patches of the synthesized impedance in (b).

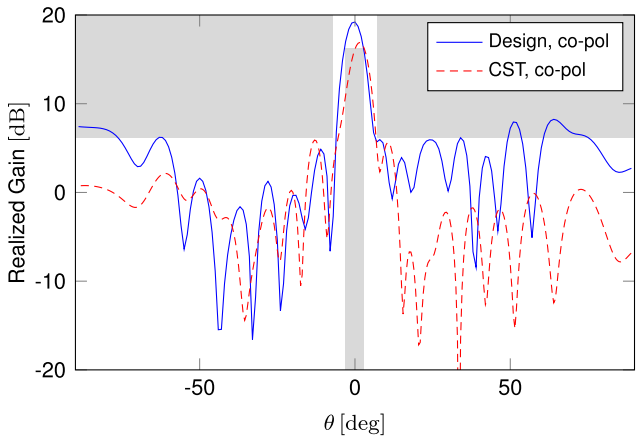

Fig. 17. Strip-like LWA, broadside radiation: comparison between the far-field pattern due to the reconstructed equivalent currents (*Design*) and the one obtained by CST simulation (*CST*), for the design without self-consistent modeling of the launching structure inside the optimization instance.

instance. There are several discrepancies in the two patterns: the main beam in the CST simulation is not directed at broadside, but tilted toward 1.5°, and there is a 2 dB loss in the realized gain, resulting in a total efficiency of 84% and an aperture efficiency of about 56%. Moreover, the side lobes toward grazing directions, predicted by the approximate design method, are significantly higher than those of the actual antenna.

These differences indicate that failing to self-consistently model the tapered PEC section inside the design algorithm forces to neglect the interaction between the launching structure and the metasurface, leading to significant inaccuracies in the final results (despite the high accuracy level in the computation of the incident field achieved by including the feeding structure).

2) Design With Self-Consistent Modeling of the Launching Structure and Cell-Wise Enforcement of PEC Constraint: We consider now both the PEC and the IBC region self-consistently in the design process, as proposed in this article; coherently with this, the incident field $\boldsymbol{E}_{\rm inc}$ is now extracted from full-wave simulations of the 3-D coaxial feed *only* [see Fig. 5(b)]. This field is shown in Fig. 18(a), while the optimized current density returned by the automated method and the corresponding impedance pattern are represented in Fig. 18(b) and (c), respectively. The synthesized impedance profile is unconventional and different from the typical sinusoidal modulation used to design 1-D LWAs [30]. Fig. 18(d) and (e) shows the physical implementation of the synthesized impedance pattern and the current density obtained from full-wave simulation of the full antenna.

The comparison between the simulated far-field pattern and the one predicted by the automated design method is shown in Fig. 19, together with the mask-type constraints imposed on the desired radiation pattern. There is excellent agreement between the two patterns: broadside radiation is achieved as

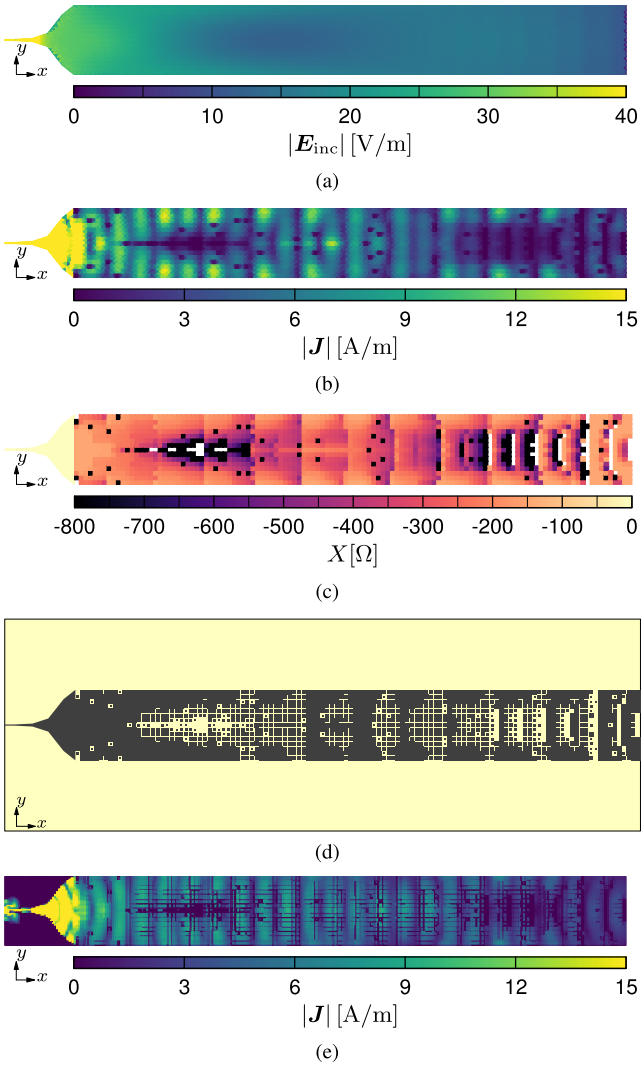

Fig. 18. Strip-like LWA, broadside radiation: design input/outputs with self-consistent modeling of the launching structure, obtained using cell-wise enforcement of PEC constraint. (a) Incident electric field, extracted from the full-wave simulation of the coaxial connector in CST. (b) Optimum current density returned as output by the design method. (c) Corresponding impedance pattern. (d) Implementation via square patches of the synthesized impedance. (e) Current density obtained simulating the actual antenna in CST.

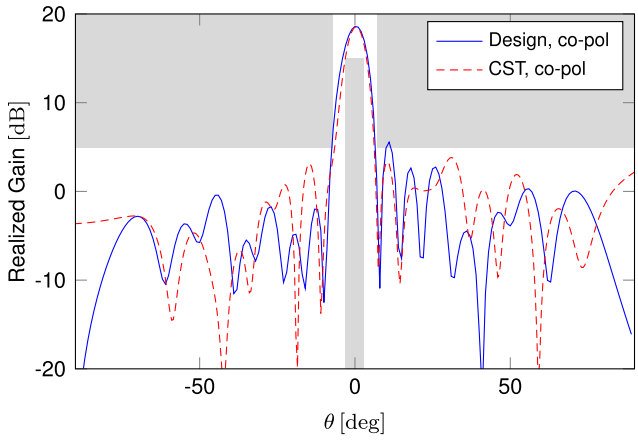

Fig. 19. Strip-like LWA, broadside radiation: comparison between the far-field pattern due to the reconstructed equivalent currents (*Design*) and the one obtained by full-wave simulation in CST (*CST*), for the self-consistent design with cell-wise enforcement of the PEC condition.

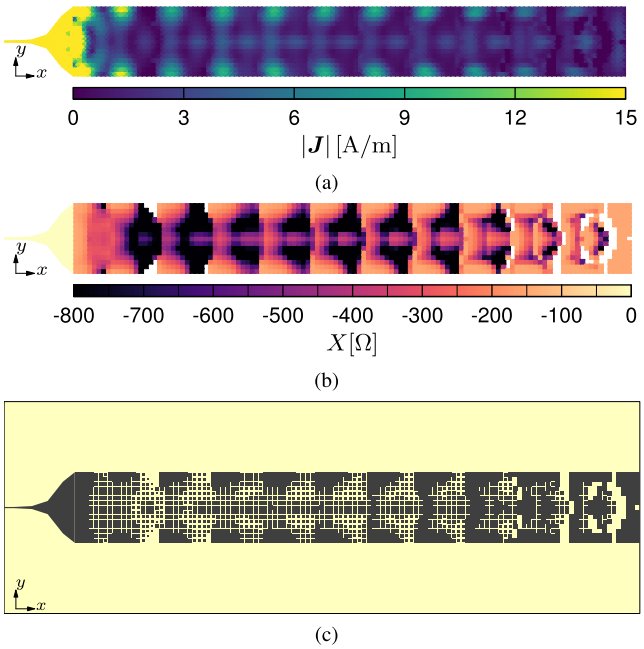

Fig. 20. Strip-like LWA, broadside radiation: design outputs for the self-consistent solution obtained with edge-wise enforcement of the PEC constraint. (a) Optimum current density returned by the design method. (b) Corresponding impedance pattern. (c) Implementation via square patches of the synthesized impedance in CST.

expected with a *realized* gain of 18.5 dB, thus effectively overcoming the open stopband problem. Although different from those of the IBC approximation, the simulated side lobes satisfy the desired SLL. The discrepancies in the pattern are mainly due to the fact that the automated design method posits an infinite dielectric substrate, while in the 3-D simulation implemented in the commercial solver, the dielectric layer is finite [see Fig. 18(d)]. A further source of differences may be traced back to the unit cell design, which is based on a local-periodicity approximation. The total efficiency shown by the simulated antenna is 92%, while the aperture efficiency is equal to 75%.

3) Design With Self-Consistent Modeling of the Launching Structure and Edge-Wise Enforcement of PEC Constraint: Finally, we carry out the same design as in Section IV-D2 using the *edge-wise* enforcement of the PEC constraint defined in (27). The optimum current density and the corresponding impedance pattern are shown in Fig. 20, together with its implementation via square patches.

The two synthesized impedance profiles in Figs. 18(c) and 20(b) show some differences, resulting in slightly different patterns; the edge-wise enforcement (see Fig. 21) appears to achieve a higher realized gain of 19.2 dB, at the expenses of a worse sidelobe profile. However, after the realization and simulation of the complete antenna with CST, the side lobes turn out to be better and actually very similar to those of the other method. The total and aperture efficiencies are 98% and 82%, respectively.

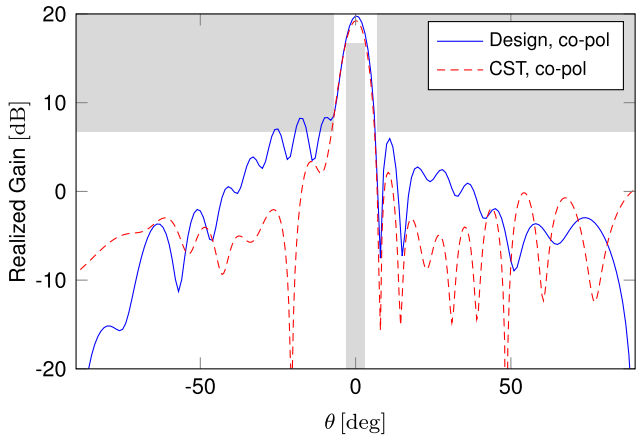

Fig. 21. Strip-like LWA, broadside radiation: comparison between the far-field pattern due to the reconstructed equivalent currents (*Design*) and the one obtained with full-wave simulation in CST (*CST*), for the design achieved by enforcing the PEC condition edge-wise.

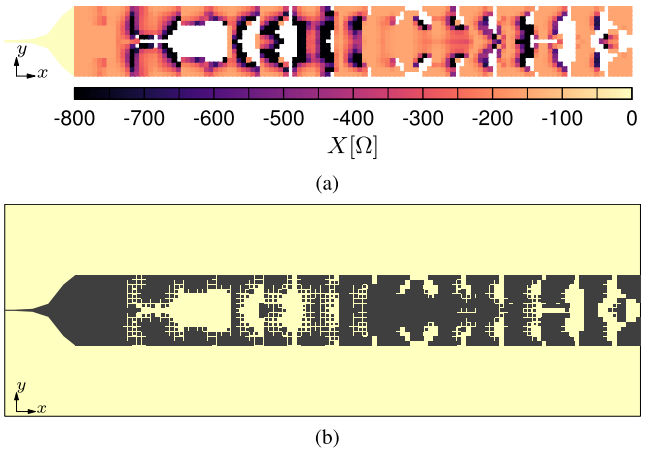

Fig. 22. Strip-like LWA, squinted beam: design outputs for the self-consistent solution obtained with cell-wise enforcement of the PEC constraint (a) synthesized impedance pattern, and (b) its implementation via square patches.

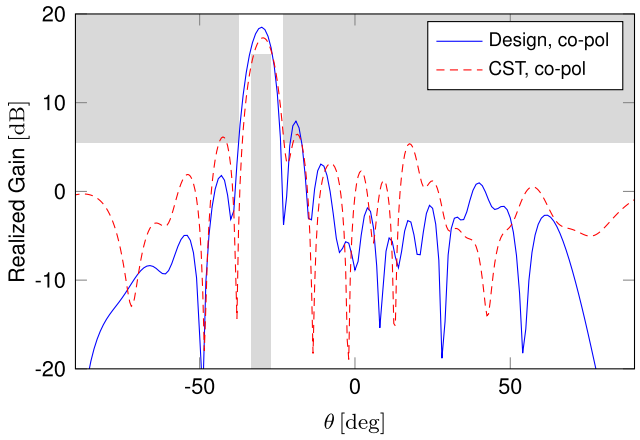

Fig. 23. Strip-like LWA, squinted beam: comparison between the far-field pattern due to the reconstructed equivalent currents (*Design*) and the one obtained with full-wave simulation in CST (*CST*).

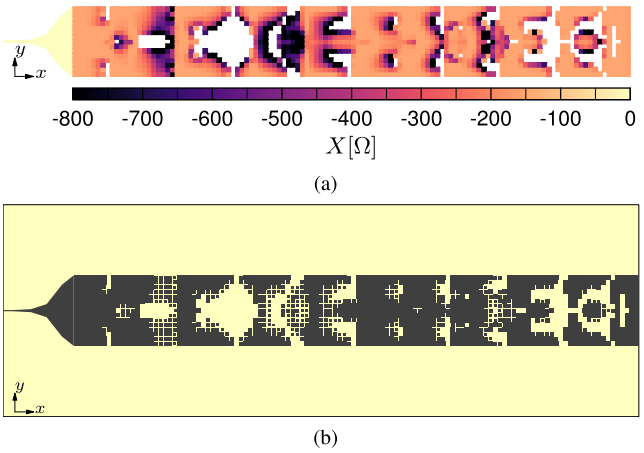

Fig. 24. Strip-like LWA, cosecant squared pattern: design outputs for the self-consistent solution obtained with cell-wise enforcement of the PEC constraint. (a) Synthesized impedance pattern, and (b) its implementation via square patches.

E. "Strip-Like" Rectangular Metasurface With Squinted Beam

The task of designing a "strip-like" antenna radiating a squinted beam is also undertaken, to demonstrate the capabilities of the proposed method. The same substrate and dimensions of the previous examples are considered, and the optimization process took again about 4 h 40 min.

The target is a $-30\,^\circ$ backward beam. The design is carried out using *cell-wise* enforcement of the PEC constraint. The synthesized impedance pattern and its geometrical implementation using square patches are shown in Fig. 22, while the far-field pattern returned by the design method and the one resulting from full-wave simulation of the complete antenna are pictured in Fig. 23, together with the far-field mask-type constraints imposed in the optimization instance. The two patterns are in excellent agreement around the main beam, with only a small drop (-1.2 dB) in the realized gain. The simulated total efficiency is 98%. There is some discrepancy in the side lobes region, that increases going farther from the main beam and can be ascribed to the finite dielectric substrate used in the simulation environment; nevertheless, the simulated side lobes abide to the SLL mask constraint.

F. "Strip-Like" Rectangular Metasurface With Cosecant Squared Pattern

Finally, we address the design of a rectangular metasurface that radiates a cosecant squared beam [24], with power pattern $D(\theta)$ defined as [7]

$$D(\theta) = \frac{\sin^2(\theta_{\min})}{\sin^2(\theta)}, \quad \theta_{\min} \le \theta \le \theta_{\max}. \tag{30}$$

We consider a case with $\theta_{\min} = 10°$, $\theta_{\max} = 40°$; radiation constraints are imposed in the principal plane $\varphi = 0°$. The admissible ripple is set at ± 2 dB from the target mask. Using the same antenna geometry of the previous examples, this optimization instance required about 4 h 40 min to complete. *Cell-wise* enforcement of the PEC constraint is employed.

The synthesized impedance pattern and its geometrical implementation using square patches are shown in Fig. 24, while the far-field pattern returned by the design method and

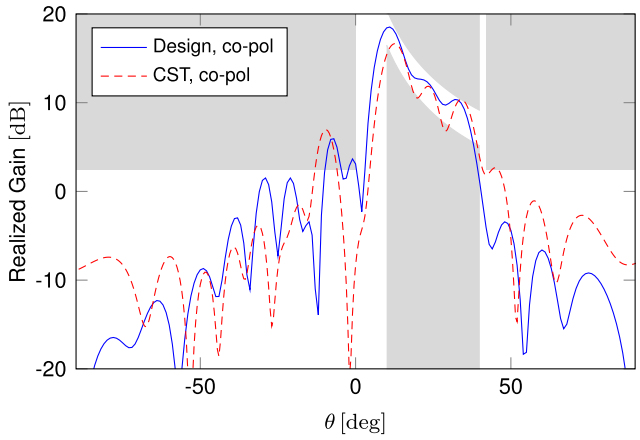

Fig. 25. Strip-like LWA, cosecant squared pattern: comparison between the far-field pattern due to the reconstructed equivalent currents (*Design*) and the one obtained with full-wave simulation in CST (*CST*).

the one resulting from full-wave simulation of the complete antenna are pictured in Fig. 25. There is good agreement between the output of the design method and the simulations results: the simulated radiation pattern abides to the mask-type constraints almost everywhere, with the exception of a small backward sidelobe that was already expected to exceed the SLL mask from the design stage. The total efficiency is 98%.

V. Conclusion

We have presented a method to self-consistently incorporate a specified PEC feeding structure in the current-only inverse design of metasurface antennas. We have shown application examples of center-fed metasurface antennas and edge-fed "strip-like" LWAs; in the latter, the feed is electrically connected to the IBC part. We have found that including the feed in the design of center-fed circular antennas is important, especially to avoid deterioration of the peak gain, in line with recent literature. Its impact on "strip-like" LWAs is significantly more pronounced, affecting the accuracy of the radiation pattern in both the main and sidelobe regions.

Appendix A
Radiated Field Functional

The cost function encompassing the radiation requirements is defined as

$$f_{\text{rad}} = w^{\text{co}}\rho^{\text{co}} + w^{\text{cx}}\rho^{\text{cx}} + w^{\text{tot}}\rho^{\text{tot}} \tag{31}$$

where each individual functional of the weighted sum is given by the sum of terms over all considered far-field directions

$$\rho^{\text{x}} = \sum_{j=1}^{N_{\text{ff}}} \rho_j^{\text{x}} \tag{32}$$

where "x" should be replaced by the corresponding component ("co", "cx" or "tot"), and the index $j = 1, \ldots, N_{\text{ff}}$ refers to the far-field direction (θ_j, ϕ_j). Below are the definitions of each term

$$\rho_j^{\text{co}} = \text{r}^2\big(M_{\text{L},j}^{\text{co}} - F_j^{\text{co}}\big) + \text{r}^2\big(F_j^{\text{co}} - M_{\text{U},j}^{\text{co}}\big) \tag{33}$$

$$\rho_j^{\text{cx}} = \text{r}^2\big(F_j^{\text{cx}} - M_j^{\text{cx}}\big) \tag{34}$$

$$\rho_j^{\text{tot}} = \text{r}^2\big(F_j^{\text{tot}} - M_j^{\text{tot}}\big) \tag{35}$$

where $\text{r}(x) = \max(x, 0)$, and

$$F_j^{\text{co}} = \big|E_j^{\text{co}}\big|^2 \tag{36}$$

$$F_j^{\text{cx}} = \big|E_j^{\text{cx}}\big|^2 \tag{37}$$

$$F_j^{\text{tot}} = \big|E_j^{\text{co}}\big|^2 + \big|E_j^{\text{cx}}\big|^2. \tag{38}$$

The co- and cross-polarization components of the electric field are obtained by applying the discretized radiation operator to the current coefficients

$$\mathsf{E}^{\text{co}} = \mathbf{R}^{\text{co}}\,\mathsf{I} \tag{39}$$

$$\mathsf{E}^{\text{cx}} = \mathbf{R}^{\text{cx}}\,\mathsf{I}. \tag{40}$$

Appendix B
Impedance Realizability Functional

The total realizability cost function for the IBC includes the conditions of passivity and losslessness ("act"), scalarity ("scal"), and upper/lower impedance bounds ("imp")

$$f_{\text{ibc}} = w^{\text{act}}\rho^{\text{act}} + w^{\text{scal}}\rho^{\text{scal}} + w^{\text{imp}}\rho^{\text{imp}}. \tag{41}$$

It is formulated as a weighted sum of functionals. Each of these functionals in turn is expressed as a sum of functionals defined over individual cells

$$\rho^{\text{x}} = \sum_{i \in \mathcal{I}_{\text{ibc}}} \rho_i^{\text{x}} \tag{42}$$

where "x" should be replaced by the corresponding condition ("act", "scal" or "imp"), and $\mathcal{I}_{\text{ibc}} = \{i \in \mathbb{N} \,|\, \mathcal{S}_i \subset \mathcal{S}_{\text{IBC}}\}$. Individual terms are defined as follows:

$$\rho_i^{\text{act}} = {\mathcal{P}_i}^2 \tag{43}$$

$$\rho_i^{\text{scal}} = \mathcal{E}_i\,\mathcal{J}_i - \big({\mathcal{P}_i}^2 + {\mathcal{Q}_i}^2\big) \tag{44}$$

$$\rho_i^{\text{imp}} = \text{r}^2(X_{\min}\mathcal{J}_i - \mathcal{Q}_i) + \text{r}^2(\mathcal{Q}_i - X_{\max}\mathcal{J}_i) \tag{45}$$

where

$$\mathcal{P}_i = \frac{1}{A_i}\,\text{Re}\iint_{\mathcal{S}_i} \boldsymbol{E}_{\tan}\cdot\boldsymbol{J}^*\,\text{d}S = \text{Re}\big(\mathsf{I}^{\text{H}}\boldsymbol{\Gamma}_i\mathsf{V}\big) \tag{46}$$

$$\mathcal{Q}_i = \frac{1}{A_i}\,\text{Im}\iint_{\mathcal{S}_i} \boldsymbol{E}_{\tan}\cdot\boldsymbol{J}^*\,\text{d}S = \text{Im}\big(\mathsf{I}^{\text{H}}\boldsymbol{\Gamma}_i\mathsf{V}\big) \tag{47}$$

$$\mathcal{J}_i = \frac{1}{A_i}\iint_{\mathcal{S}_i} |\boldsymbol{J}|^2\,\text{d}S = \mathsf{I}^{\text{H}}\boldsymbol{\Gamma}_i\mathsf{I} \tag{48}$$

$$\mathcal{E}_i = \frac{1}{A_i}\iint_{\mathcal{S}_i} |\boldsymbol{E}_{\tan}|^2\,\text{d}S = \mathsf{V}^{\text{H}}\boldsymbol{\Gamma}_i\mathsf{V} \tag{49}$$

with A_i being the surface area of the ith cell. In the above

$$\mathsf{V} = \mathbf{G}^{-1}(\mathsf{V}_{\text{inc}} + \mathbf{L}\mathsf{I}) \tag{50}$$

where $\mathbf{G} \in \mathbb{R}^{N\times N}$ is the Gram matrix of the RWG basis functions, defined as

$$(\mathbf{G})_{mn} = \iint \boldsymbol{\Lambda}_m(\boldsymbol{r})\cdot\boldsymbol{\Lambda}_n(\boldsymbol{r})\,\text{d}\boldsymbol{r} \tag{51}$$

and $\mathbf{\Gamma}_i \in \mathbb{R}^{N\times N}$ is the (averaging) local Gram matrix for the ith cell, defined as

$$(\mathbf{\Gamma}_i)_{mn} = \frac{1}{A_i}\iint_{\mathcal{S}_i} \mathbf{\Lambda}_m(\boldsymbol{r})\cdot\mathbf{\Lambda}_n(\boldsymbol{r})\,\mathrm{d}\boldsymbol{r}. \tag{52}$$

APPENDIX C
IMPEDANCE CALCULATION FROM THE CURRENT

Starting from the discretized integral equation (6) restricted to the IBC region, the impedance is first expanded into a linear combination of basis functions

$$Z(\boldsymbol{r}) = \sum_{i=1}^{M} z_i\,\psi_i(\boldsymbol{r}). \tag{53}$$

From the knowledge of the (optimal) equivalent current, the coefficients of the impedance expansion are found by minimizing the error in the integral equation, i.e.,

$$\mathsf{z} = \underset{\mathsf{z}\in\mathbb{C}^M}{\arg\min}\,\|\mathsf{V}_{\mathrm{tot}} - \mathbf{\Psi}\mathsf{z}\| \tag{54}$$

where z collects the impedance coefficients, $\mathsf{V}_{\mathrm{tot}} = \mathsf{V}_{\mathrm{inc}} + \mathbf{L}\mathsf{I}$ is the total electric field in terms of the equivalent current, and the elements of the matrix $\mathbf{\Psi}$

$$(\mathbf{\Psi})_{mi} = \langle\, \mathbf{\Lambda}_m\,,\, \psi_i\, \boldsymbol{J}^{\Lambda}\,\rangle \tag{55}$$

with $\boldsymbol{J}^{\Lambda} = \sum_{n=1}^{N} I_n\mathbf{\Lambda}_n$, represent the linear dependence of the total field on the coefficients of the impedance. Finding the impedance through (54) constitutes a convex optimization problem.

If we express the impedance in terms of piecewise constant basis functions on each triangle, i.e.,

$$\psi_i(\boldsymbol{r}) = \begin{cases} 1, & \text{for } \boldsymbol{r}\in\mathcal{S}_i \\ 0, & \text{elsewhere} \end{cases}, \quad i = 1,\ldots,N_{\mathrm{c}} \tag{56}$$

the optimum impedance coefficients can be obtained in closed form as

$$z_i = \frac{\iint_{\mathcal{S}_i}\boldsymbol{E}_{\tan}\cdot\boldsymbol{J}^*\,\mathrm{d}S}{\iint_{\mathcal{S}_i}|\boldsymbol{J}|^2\,\mathrm{d}S} = \frac{\mathsf{I}^{\mathsf{H}}\mathbf{\Gamma}_i\mathsf{V}}{\mathsf{I}^{\mathsf{H}}\mathbf{\Gamma}_i\mathsf{I}}. \tag{57}$$

A limiting case, often encountered in practice, is when the denominator of (57) is close to zero, while its numerator is much larger than zero, which corresponds to an infinite impedance value. This implies the absence of the IBC over the considered triangle, a condition that can be easily implemented in the numerical solution by removing the corresponding degrees of freedom from the discretization.

REFERENCES

[1] G. Minatti et al., "Modulated metasurface antennas for space: Synthesis, analysis and realizations," *IEEE Trans. Antennas Propag.*, vol. 63, no. 4, pp. 1288–1300, Apr. 2015.

[2] G. Minatti, F. Caminita, E. Martini, M. Sabbadini, and S. Maci, "Synthesis of modulated-metasurface antennas with amplitude, phase, and polarization control," *IEEE Trans. Antennas Propag.*, vol. 64, no. 9, pp. 3907–3919, Sep. 2016.

[3] M. Bodehou, C. Craeye, and I. Huynen, "Electric field integral equation-based synthesis of elliptical-domain metasurface antennas," *IEEE Trans. Antennas Propag.*, vol. 67, no. 2, pp. 1270–1274, Feb. 2019.

[4] A. Scarabosio, F. Verni, M. Righero, G. Giordanengo, and G. Vecchi, "Toward fast machine design of metasurface antennas," in *Proc. 16th Eur. Conf. Antennas Propag.*, Madrid, Spain, Mar. 2022, pp. 1–4.

[5] F. Verni, "Advanced computational electromagnetics for metasurfaces," Ph.D. dissertation, Dept. Electron. Telecommun. (DET), Politecnico di Torino, Turin, Italy, Aug. 2020.

[6] J. Cavillot, M. Bodehou, and C. Craeye, "Metasurface antennas design: Full-wave feeder modeling and far-field optimization," *IEEE Trans. Antennas Propag.*, vol. 71, no. 1, pp. 39–49, Jan. 2023.

[7] M. Zucchi, F. Vernì, M. Righero, and G. Vecchi, "Current based automated design of realizable metasurface antennas with arbitrary pattern constraints," *IEEE Trans. Antennas Propag.*, vol. 71, no. 6, pp. 4888–4902, Jun. 2023.

[8] A. Epstein and G. V. Eleftheriades, "Synthesis of passive lossless metasurfaces using auxiliary fields for reflectionless beam splitting and perfect reflection," *Phys. Rev. Lett.*, vol. 117, no. 25, Dec. 2016, Art. no. 256103.

[9] V. G. Ataloglou and G. V. Eleftheriades, "Arbitrary wave transformations with Huygens' metasurfaces through surface-wave optimization," *IEEE Antennas Wireless Propag. Lett.*, vol. 20, no. 9, pp. 1750–1754, Sep. 2021.

[10] M. Salucci, A. Gelmini, G. Oliveri, N. Anselmi, and A. Massa, "Synthesis of shaped beam reflectarrays with constrained geometry by exploiting nonradiating surface currents," *IEEE Trans. Antennas Propag.*, vol. 66, no. 11, pp. 5805–5817, Nov. 2018.

[11] T. Brown, Y. Vahabzadeh, C. Caloz, and P. Mojabi, "Electromagnetic inversion with local power conservation for metasurface design," *IEEE Antennas Wireless Propag. Lett.*, vol. 19, no. 8, pp. 1291–1295, Aug. 2020.

[12] T. Brown and P. Mojabi, "Cascaded metasurface design using electromagnetic inversion with gradient-based optimization," *IEEE Trans. Antennas Propag.*, vol. 70, no. 3, pp. 2033–2045, Mar. 2022.

[13] J. Budhu and A. Grbic, "Perfectly reflecting metasurface reflectarrays: Mutual coupling modeling between unique elements through homogenization," *IEEE Trans. Antennas Propag.*, vol. 69, no. 1, pp. 122–134, Jan. 2021.

[14] J. Budhu, E. Michielssen, and A. Grbic, "The design of dual band stacked metasurfaces using integral equations," *IEEE Trans. Antennas Propag.*, vol. 70, no. 6, pp. 4576–4588, Jun. 2022.

[15] M. Bodehou, C. Craeye, E. Martini, and I. Huynen, "A quasi-direct method for the surface impedance design of modulated metasurface antennas," *IEEE Trans. Antennas Propag.*, vol. 67, no. 1, pp. 24–36, Jan. 2019.

[16] F. Caminita, E. Martini, G. Minatti, M. Sabbadini, and S. Maci, "Low-profile dual-polarized isoflux antennas for space applications," *IEEE Trans. Antennas Propag.*, vol. 69, no. 6, pp. 3204–3213, Jun. 2021.

[17] M. Bodehou and C. Craeye, "Array surface-wave launcher for the efficient generation of shaped beam and multibeam with metasurface," *IEEE Trans. Antennas Propag.*, vol. 69, no. 12, pp. 8860–8865, Dec. 2021.

[18] L. Teodorani, M. Zucchi, and G. Vecchi, "Modeling of 3D feeding structures in the automated design of metasurface antennas," in *Proc. 18th Eur. Conf. Antennas Propag.*, Glasgow, U.K., Mar. 2024, pp. 1285–1287.

[19] E. F. Kuester, M. A. Mohamed, M. Piket-May, and C. L. Holloway, "Averaged transition conditions for electromagnetic fields at a metafilm," *IEEE Trans. Antennas Propag.*, vol. 51, no. 10, pp. 2641–2651, Oct. 2003.

[20] K. A. Michalski and J. R. Mosig, "Multilayered media green's functions in integral equation formulations," *IEEE Trans. Antennas Propag.*, vol. 45, no. 3, pp. 508–519, Mar. 1997.

[21] S. Rao, D. Wilton, and A. Glisson, "Electromagnetic scattering by surfaces of arbitrary shape," *IEEE Trans. Antennas Propag.*, vol. AP-30, no. 3, pp. 409–418, May 1982.

[22] K. A. Michalski, "Electromagnetic field computation in planar multilayers," in *Encyclopedia of RF and Microwave Engineering*. Hoboken, NJ, USA: Wiley, 2005.

[23] J. Nocedal and S. J. Wright, *Numerical Optimization* (Springer Series in Operations Research), 2nd ed. New York, NY, USA: Springer, 2006.

[24] *IEEE Standard for Definitions of Terms for Antennas*, IEEE Standard 145-2013 Revis. IEEE Standard 145-1993, Mar. 2014, pp. 1–50.

[25] D. H. Brandwood, "A complex gradient operator and its application in adaptive array theory," *IEE Proc. H-Microw. Opt. Antennas*, vol. 130, no. 1, pp. 11–16, 1983.

[26] R. Maggiora, G. Vecchi, V. Lancellotti, and V. Kyrytsya, "Efficient 3D/1D self-consistent integral-equation analysis of ICRH antennae," *Nucl. Fusion*, vol. 44, no. 8, p. 846, Jul. 2004.

[27] W. C. Chew, Z. Nie, Q. H. Liu, and Y. T. Lo, "Analysis of a probe-fed microstrip disk antenna," *IEE Proc. H-Microw., Antennas Propag.*, vol. 138, no. 2, pp. 185–191, Apr. 1991.
[28] G. Minatti, E. Martini, and S. Maci, "Efficiency of metasurface antennas," *IEEE Trans. Antennas Propag.*, vol. 65, no. 4, pp. 1532–1541, Apr. 2017.
[29] *CST Studio Suite*, Dassault Systèmes, France, 2022.
[30] A. M. Patel and A. Grbic, "A printed leaky-wave antenna based on a sinusoidally-modulated reactance surface," *IEEE Trans. Antennas Propag.*, vol. 59, no. 6, pp. 2087–2096, Jun. 2011.
[31] F. Vernì, M. Righero, and G. Vecchi, "On the use of entire-domain basis functions and fast factorizations for the design of modulated metasurface," *IEEE Trans. Antennas Propag.*, vol. 68, no. 5, pp. 3824–3833, May 2020.
[32] A. Oliner and A. Hessel, "Guided waves on sinusoidally-modulated reactance surfaces," *IRE Trans. Antennas Propag.*, vol. 7, no. 5, pp. 201–208, Dec. 1959.
[33] D. R. Jackson, C. Caloz, and T. Itoh, "Leaky-wave antennas," *Proc. IEEE*, vol. 100, no. 7, pp. 2194–2206, Jul. 2012.

Lucia Teodorani (Member, IEEE) received the B.Sc. degree in electronics engineering for energy and information from the University of Bologna (Cesena Campus), Cesena, Italy, in 2016 and the M.Sc. degree in electronics engineering from the Politecnico di Torino, Turin, Italy, in 2020, where she is currently pursuing the Ph.D. degree in electrical, electronics and communication engineering.

Her research interests include advanced automated methods for the deterministic design of metasurface antennas and the development of fixed-frequency reconfigurable antennas employing lumped active components or liquid crystals.

Marcello Zucchi (Member, IEEE) received the B.Sc. degree in electronics and telecommunications engineering from the University of Bologna, Bologna, Italy, in 2014, the M.Sc. degree in electronics engineering and the Ph.D. degree in electrical, electronics and communications engineering from the Politecnico di Torino, Turin, Italy, in 2018 and 2022, respectively.

In 2023, he joined the Department of Electronics and Telecommunications, Politecnico di Torino, as a Post-Doctoral Researcher. His research interests include global optimization algorithms for flat antenna design, automatic synthesis of metasurface antennas, and field focusing algorithms for hyperthermia treatment.

Giuseppe Vecchi (Life Fellow, IEEE) received the Laurea and Ph.D. degrees in electronic engineering from the Politecnico di Torino, Turin, Italy, in 1985 and 1989, respectively, with doctoral research carried out partly at Polytechnic University, Farmingdale, NY, USA.

He was a Visiting Scientist with Polytechnic University, from 1989 to 1990. He was an Associate Professor at the Politecnico di Torino, from 1992 to 2000. Since 1990, he has been with the Department of Electronics, Politecnico di Torino, as an Assistant Professor and a Professor since 2000. He was a Visiting Scientist with the University of Helsinki, Helsinki, Finland, in 1992, and has been an Adjunct Faculty Member with the Department of Electrical and Computer Engineering, University of Illinois at Chicago, Chicago, IL, USA, from 1997 to 2011. Since 2015, he has been serving as the Director of the Antenna and EMC Laboratory (LACE), Politecnico di Torino. His current research activities concern analytical and numerical techniques for design, measurement and diagnostics of antennas and devices, medical applications, and imaging.

Prof. Vecchi is a member of the Board of the European School of Antennas (ESOA), the IEEE Antennas and Propagation Standard Committee, and the IEEE-APS Educational Committee. He has been an Associate Editor of the IEEE TRANSACTIONS ON ANTENNAS AND PROPAGATION, the Chairperson of the IEEE AP/MTT/ED Italian joint Chapter.

Open Access funding provided by 'Politecnico di Torino' within the CRUI CARE Agreement